Capillarity

Vol. 4, No. 4, p. 76-86, 2021

Original article

A microfluidic study of transient flow states in permeable media using fluorescent particle image velocimetry

Jindi Sun[1], Ziqiang Li[2], Frederico Furtado[2], Saman A. Aryana[1,2]*

[1]*Department of Chemical Engineering, University of Wyoming, Laramie, WY 82071, USA*
[2]*Department of Mathematics and Statistics, University of Wyoming, Laramie, WY 82071, USA*

Keywords:
Particle image velocimetry
transition state
permeable media
microfluidics

Cited as:
Sun, J., Li, Z., Furtado, F., Aryana, S. A. A microfluidic study of transient flow states in permeable media using fluorescent particle image velocimetry. Capillarity, 2021, 4(4): 76-86, doi: 10.46690/capi.2021.04.03

Abstract:
Velocity fields in flow in permeable media are of great importance to many subsurface processes such as geologic storage of CO_2, oil and gas extraction, and geothermal systems. Steady-state flow is characterized by velocity fields that do not change significantly over time. The flow field transitions to a new steady state once it experiences a disturbance such as a change in flow rate or in pressure gradient. This transition is often assumed to be instantaneous, which justifies the expression of constitutive relations as functions of instantaneous phase saturations. This work examines the evolution of velocity fields in a surrogate quasi-2D permeable medium using a microfluidic device, a microscopy system, and a high-speed camera. Tracer particles are injected into the medium along with Deionized water. The evolution of the velocity field is examined by tracing these particles in the captured images using the standard high-density particle image velocimetry algorithm founded on cross-correlation. The results suggest that the transition between steady states for an incompressible fluid takes a finite and non-negligible amount of time that is independent of the magnitude of the change in pressure gradient. The existence of transient states and the nature of the response during these states are readily interpreted by the principle of least action where flow gradually establishes an optimal configuration such that energy dissipation is minimized. The findings provide evidence against the applicability of the assumption that flowing phases relax instantaneously to their steady states and, hence, against the accuracy of the classical multiphase extension of Darcy's law.

1. Introduction

Models for macro-scale permeable media often rely on some form of Darcy's law as the conservation of momentum (Aryana and Kovscek, 2012). Darcy's law provides a linear relation between the gradient of the field potential (e.g., hydraulic head or pressure) and the macroscale (Darcy) velocity (Whitaker, 1986). This linear relation is strictly valid for single-phase flows under low-Reynolds number and steady-state conditions where fluid inertia may be reasonably neglected (Hubbert, 1957; Dullien, 2012). Permeability is the constant of proportionality for this linear relation and its symmetricity is predicated in part on steady flows (King et al., 1995). Darcy's law is extended to simultaneous flows of multiple phases via the use of constitutive relations, i.e., relative phase permeabilities and capillary pressure. Many instances of the use of this extension, however, include unsteady flows (Wang et al., 2018), such as early stages of capillary imbibition of a permeable rock and fluid mixing near oil-water displacement fronts (Wang et al., 2020).

Capillary pressure and relative permeabilities are often expressed as functions of local phase saturations (Aryana and Kovscek, 2013; Chao et al., 2021). Since saturation is defined over a representative elementary volume (REV), the assumption that sub-REV fluid configurations relax instantaneously to their steady states is the underlying premise for Darcy's law and its classical multiphase extension (Barenblatt et al., 2003). To bring Darcy's law and its multiphase extensions in accord with its underlying assumption of near-steady flows, one may include dynamic compact spatial support for

Yandy Scientific Press

*Corresponding author.
E-mail address: jsun6@uwyo.edu (J. Sun); zli11@uwyo.edu (Z. Li); Furtado@uwyo.edu (F. Furtado); saryana@uwyo.edu (S. A. Aryana).

Received October 5, 2021; revised October 25, 2021; accepted October 25, 2021; available online October 26, 2021.

the constitutive relations (Wang et al., 2019). These length scales arise from rapid fluctuations in rock properties and fluid saturations attributable to heterogeneity and nonlinearity (Wang et al., 2020). This work aims to show the presence of finite and non-negligible unsteady-state periods that mark the transition between steady-state flow states by examining single-phase flow in a permeable medium. The premise is that these transition regimes, if present in the simplest of cases: Flow of single-phase water in a permeable medium, are of consequence in permeable media in general, and their presence would support the multiscale formulation proposed by Wang et al. (2019). As such, the macroscale conservation laws are fundamentally multi-scale, and a careful consideration of their multiscale nature is a pre-requisite for their formulation.

In this work, a microfluidic device in conjunction with optical microscopy is used to track the flow of neutrally buoyant microspheres inside a surrogate permeable medium and examine the transition between steady flow states. A microfluidic device, in the context of flow experiments through permeable media, is a miniaturized system with micrometric channels in which one or more types of fluids flow (Tabeling, 2005). Traditionally, one would conduct flow experiments on real geological media (e.g., core samples) to gain insight into subsurface flow behavior (Liu et al., 2019). Such experiments would allow an injection fluid to permeate through actual subsurface geometry at the expense of causing permanent alteration to the geometry and chemistry of flow channels. The resulting analysis may not be reproduced in subsequent reruns of the same experiment. A workaround to this issue is to substitute core samples with microfluidic devices that are both chemically inert to the injection fluid and reflective of the subsurface geometry. Microfluidic devices therefore allow flow experiments to be conducted in rapid succession with full reproducibility. This study uses a microfluidic device with a quasi-2D representation of a real sandstone geometry (Guo and Aryana, 2016, 2019) to investigate the existence of non-negligible transition flow states. The reproducibility of flow experiments using microfluidic devices facilitates the repeated, imaging-based analysis of fluid flows that are subject to changes in flow parameters. The captured image sequences are analyzed to reconstruct the velocity fields. Quantitative analysis of these fields enables exploration of flow states and investigation of the potential existence of transient states.

1.1 Microfluidic device

Microfluidic devices provide an ideal and cost-efficient platform to study fluid kinematics. The fabrication of microfluidic devices and its applications have gradually matured over the recent decades (Mijatovic et al., 2005). Prominent examples include the study of blood vessels (Lima, 2008) and neural stem cells (Chung et al., 2005) in the field of biomedical engineering. In this research, the microfluidic study of fluid flow is facilitated by the selection of a transparent material, i.e., glass. As a surrogate of the subsurface formation, glass allows the fluids enclosed within to undergo different flow, pressure and temperature conditions while being directly observed through digital imaging techniques. The flow network used in this work is based on a map of a sandstone that is previously described by Guo and Aryana (2016, 2019). The map of the pore network is informed by Scanning electron microscopy images of a thin section of a sample of rock where pore spaces are connected based on throat size distribution data obtained from a mercury intrusion experiment.

1.2 Flow states

The state of fluid flow may be categorized using different metrics. For the purpose of this study, fluid flow will be categorized in the kinematic sense as either being in a steady state or being in a transient state. A steady state is defined as a flow state where the time-derivative of its velocity field is identically zero, whereas a transient state is defined as a flow state where the velocity field has a non-vanishing time derivative. Once a sudden external perturbation is applied to a steady-state flow, the flow leaves this steady state and enter a transient state, and eventually settles into another steady state after a lapse of time. In this microfluidic study, once an initial steady flow state is established, a persistent increase in the inlet pressure is applied to force the flow into a transient state. This transient state is characterized via analysis of images captured at a high frame rate, and the influence of the magnitude of pressure change on its duration is explored.

1.3 Fluorescent particle image velocimetry

Particle image velocimetry (PIV) refers to the experimental setup and analysis methods used to determine the instantaneous velocity field in a flowing fluid. PIV has been developed and used in many fields of study (Tauro et al., 2012; Li et al., 2018), including a microfluidic study similar to the present one on tubing flow (Shinohara et al., 2004).

Image-based study of fluid flow within microfluidic devices is flexible, scalable, and well-established (Santiago et al., 1998; Adrian, 2005; Ergin et al., 2018; Li et al., 2021). The method typically uses high-speed, high-resolution camera systems to record fluid flow for later image pre-processing, segmentation, analysis, and post-processing. Neutrally buoyant fluorescent particles that do not affect the flow field are used to mark different solid or fluid phases. In high-density PIV systems, cross-correlation serves as the statistical foundation for reconstruction of the velocity field.

Fluorescent PIV, as a subset of PIV methods, quantifies the position or displacement of neutrally buoyant fluorescent tracker particles that accurately trace the motion of the fluid (Northrup et al., 1991; Unadkat et al., 2009). A digital PIV system consists of two parts: the acquisition of digital images and the reconstruction of the velocity field (Elsinga and Scarano, 2014; Thielicke and Stamhuis, 2014). In the acquisition step, high-speed cameras record a volume of interest at a high resolution through a microscope such that the location of tracer particles are recorded (Kvon et al., 2014). This step generates a large quantity of high-resolution images. In the reconstruction step, an efficient algorithm processes the images and generates a velocity field. Reconstruction algorithms are usually classified as low- or high-density algorithms (Unadkat et al., 2009; Adrian and Westerweel, 2011) depending on the

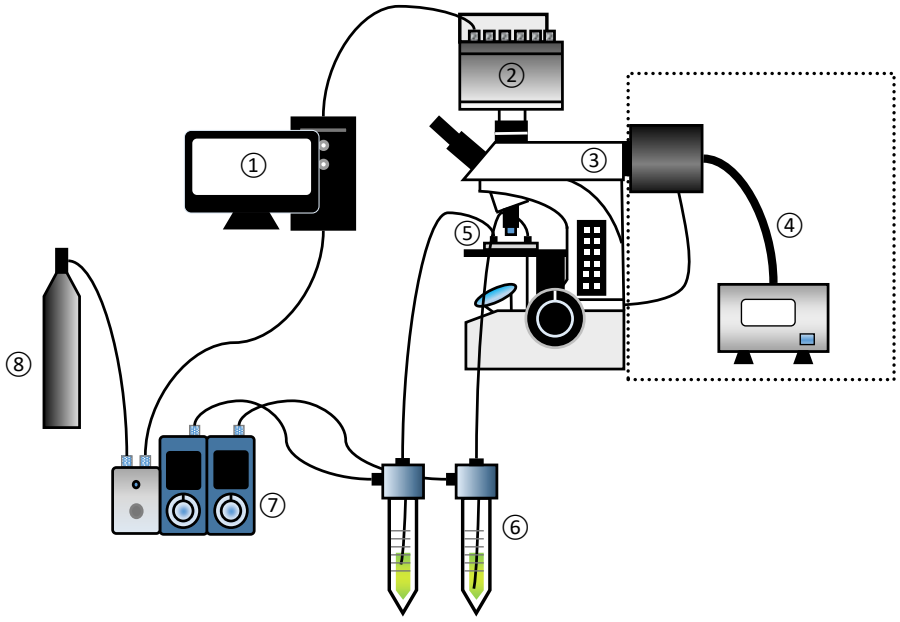

Fig. 1. The schematic of the microfluidic study. The labeled components are: ① Workstation; ② Phantom VEO 440L High Speed CMOS Monochromatic Camera; ③ Olympus BX51 TF Microscope; ④ Olympus Microscope Fluorescence 100W with Mercury Lamp U-LH100HGAPO & Power; ⑤ Micromodel; ⑥ Fluigent P-Cap Reservoirs; ⑦ Fluigent Lineup Link & Lineup Push-Pull Pressure Controller; ⑧ Nitrogen gas tank.

average particle density in each frame.

This study makes use of a basic high-density PIV algorithm based on cross-correlation (Adrian and Westerweel, 2011) and exemplifies a quantitative indicator of transient flow derivable from the reconstructed velocity field. As a final step, statistical ensembles of multiple reruns of identical experiments are used to lower the influence of random noise commonly attributed to the experiment itself and the statistical nature of high-density PIV algorithms.

2. Experiments

This section provides details regarding the microfluidic device, fluorescent particles, optical setup, and data collection (Fig. 1). The experiments are designed to enable the collection of high-quality image data for further analysis .

2.1 Fabrication

The process to fabricate the model used in this paper is similar to that described in (Guo and Aryana, 2016; Hosseini et al., 2020). A schematic of the fabrication process is provided as Fig. 2. First, a mask is created by printing transparent channels and a solid matrix onto a transparent film. The transparent channels allow light to pass through the mask while the solid matrix blocks out the light. The design of the microfluidic device contains two parts: Permeable medium and distribution channels. The permeable medium is based on a real sandstone geometry and measures 0.5 × 0.5 inch. The distribution channels are designed in accordance with Murray's law (Murray, 1926) to minimize the work of fluid circulation and shear stress. Two injection ports are created on each side of the device. The fluid is injected from one port and flows through the distribution channels before entering the permeable medium. The chip is fabricated using borosilicate

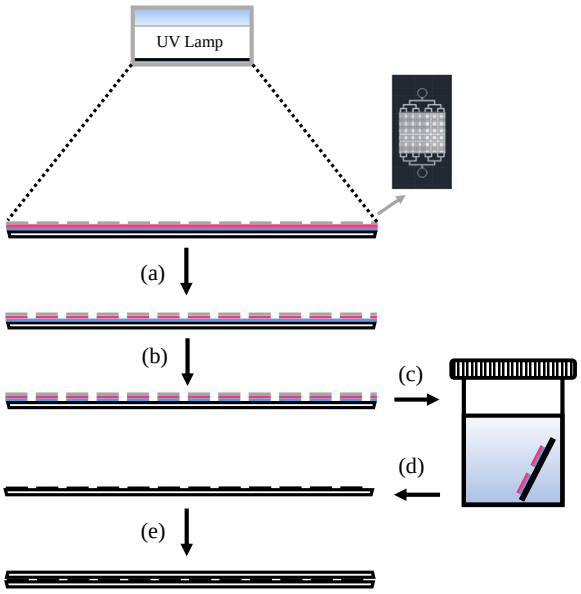

Fig. 2. The fabrication process of a micromodel starting with (a) the exposure, to a custom UV lamp, of a substrate covered with a transparent mask. The chrome layer is then (b) etched by a chrome etchant solution and subsequently (c) submerged into a BD etchant solution. Next, the substrate is (d) taken out from the solution for the subsequent cleanup of photoresist and chrome residue. As the last step, the substrate is (e) thermal bonded with a borosilicate glass plate.

glass and a photo lithography technique (Berkowski et al., 2005). The substrate comes with a layer of photoresist and a layer of chrome. Next, the substrate is covered with the transparent mask so that the pattern is transferred to the photoresist layer through its exposure to a custom UV lamp (Erickstad et al., 2015). After that, the mask is removed, and the chrome layer is etched using a chrome etchant solution.

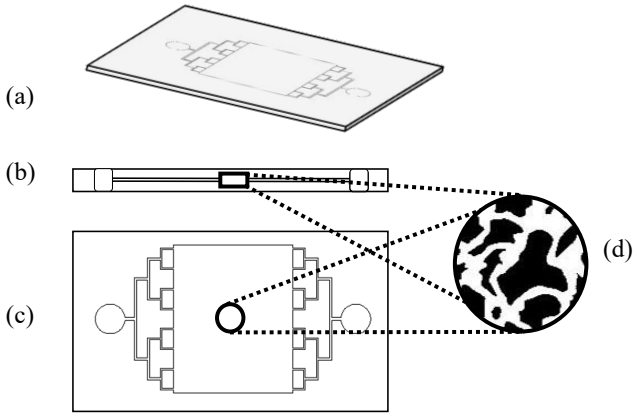

Fig. 3. Illustration of the (a) microfluidic model with its (b) side view and (c) top-down view. The (d) recorded domain of interest (a circle with a diameter of 2.2 mm) is small compared to the entire medium (15 mm long and 20 mm wide), but allows individual fluorescent particles to be observed and contains a reasonable amount of microchannels such that the domain is representative of the permeable medium.

The substrate is then wet etched by a BD Etchant (TRANSENE) to form an average channel depth of 20 μm. Finally, the substrate is thermally bonded with a blank substrate with two functional injection ports that are created using a sandblaster (Vaniman Problast).

2.2 Optical setup

A high-speed camera (Phantom VEO 440L High Speed CMOS Camera) is mounted on a fluorescent microscope (Olympus BX51 TF Microscope) that is connected to a mercury lamp (Mercury Lamp U-LH100HGAPO). The filter cube in the microscope is an Olympus Alexa Fluor 488. The microfluidic device has two ports that are indirectly connected to two pressure controllers (Fluigent Lineup Link & Lineup Push-Pull Pressure Controller) through two reservoir tubes that contain fluorescent microsphere solutions (ThermoFisher Scientific FluoSpheres®, Fluorescent Microspheres yellow-green). The role of the pressure controller is to inject nitrogen gas into the reservoir tube, which displaces the solution into the microfluidic device. Both the pressure controllers and the camera are controlled by their respective vendor software installed on the workstation. The recorded area of interest, in relation to the microfluidic device, is shown in Fig. 3. For a detailed list of instrument models, refer to the schematic of the experimental process shown in Fig. 1.

2.3 Fluorescent microsphere solution

The fluorescent particles used in this microfluidic study are the yellow-green Carboxylate-Modified FluoSpheres® with excitation/emission maxima of 505/515 nm and diameter of 1 μm supplied by ThermoFischer Scientific in the form of a water suspension at 2% solids. The fluorescent particles are excited by the light from the mercury lamp and the reflected emission light of a specific wavelength is detected and captured by the camera (Kubitscheck, 2017). By using the fluorescent property of the microspheres, the camera can capture the movement of the particles without the obstruction of the matrix. After being diluted to 0.01% solids, a single drop of Tween 80 Surfact-Amps Detergent Solution is then added to prevent the aggregation of the fluorescent particles. The mixture finally undergoes 10 seconds of sonication in an ultrasonic water bath in order to disperse the microspheres.

Table 1. Pressure profile and frame rate used in each set of experiments.

Set #	p_i' (mbar)	Δp (mbar)	Frame rate (fps)
S1	110	10	100
S2	120	20	100
S3	140	40	200
S4	180	80	200
S5	260	160	200
S6	420	320	200
S7	740	640	200
S8	1380	1280	400
T1	150	100	100
T2	250	200	100
T3	350	300	200
T4	450	400	200
T5	550	500	200
T6	650	600	200
T7	750	700	200
T8	850	800	200
T9	950	900	200
T10	1050	1000	400

Note: the outlet pressure is 50 mbar; the initial injection pressure, $p_i = 100$ mbar; the final injection pressure p_i'; the increase to injection pressure $\Delta p = p_i' - p_i$.

2.4 Injection process

The injection process in this microfluidic study takes into consideration the usage of different light sources, the need to record high-fps videos, and the methodology of statistical ensembles. The pressure profile used in each set of experiments is detailed in Table 1.

The injection procedure is described step-by-step below:

1) Configure the microscope to use its own regular light source and confirm, through visual inspection, that the microfluidic device has been saturated with the fluorescent microsphere solution.
2) Maintain a steady-state flow at an injection pressure of 100 mbar and an outlet pressure of 50 mbar.
3) Configure the microscope to use the mercury lamp.
4) Start to record video of the desired area in the microfluidic device and raise the inlet pressure by Δp in accordance with Table 1.
5) Keep on recording until the flow reaches a new steady state as confirmed by visual inspection.
6) Repeat each experiment three times.

At the beginning of each individual experiment, the injec-

tion at the inlet port must be conducted slowly to avoid the introduction of air bubbles into the permeable media. As is the case with many displacement processes, air bubbles are challenging to remove from the system. Alternating injection between the two ports assists with the removal of air bubbles. The air bubbles that persist through several cycles of alternating injection rarely move during the actual experiment and may be treated as part of the matrix without affecting data processing.

The actual recording time of each injection process takes no longer than 1 min, but the time required to transfer the data from the on-board memory to a secondary storage device takes much longer due to the large file size. After a series of experiments are completed and the associated files are transferred from the camera, the fluorescent microspheres might aggregate and require another pass of sonication to be evenly dispersed. Prior to each recording session, the pressure must be reset to 100 mbar at the inlet and 50 mbar at the outlet and maintained for at least 1 min to fully establish a steady flow in the microfluidic device.

2.5 Data collection

The selection of the video recording speed in terms of frame rates per second (fps), the video resolution in terms of pixels per frame, and the duration of the recorded video are all constrained by the on-board memory and the available presets of the recording camera. For a fixed duration of recording, it is desirable to increase the video resolution at the expense of the video recording speed, but the accuracy of a high-density PIV algorithm decreases as the average displacement of particles increases between each two adjacent frames, and the PIV algorithm does not work correctly when the fps falls below a certain threshold.

This study employs a Phantom VEO 440L High Speed CMOS Camera with the capability to record 2560 × 1600 videos at a maximum rate of 1100 fps for 11 seconds. By lowering the recording speed and fixing the resolution, the duration becomes longer. The setting of 1100 fps is not ideal for this microfluidic study for two major reasons:

1) The observation suggest that each recording must last at least 20 seconds so that the transient behavior of fluid flow is fully captured.
2) An excessively high frame rate decreases the accuracy of a basic PIV algorithm that neither calculates sub-pixel displacement nor employs a multiframe approach that is based on central difference.

The actual fps used in each set of flow experiments is determined based on the magnitude of the increase in the injection pressure as shown in Table 1.

3. Data processing

This section the steps required to reproduce the results of this microfluidic study such as image preprocessing, the configuration of a basic high-density PIV algorithm, and the quantification of the evolution of a velocity field.

3.1 Image preprocessing

Each recorded video is output by the camera as a single file encoded in the phantom cine file format. To facilitate the preprocessing of each individual frame, the open-source software ffmpeg is used to convert the .cine files to sequences of individual image files. As a reminder, a sequence of images may easily occupy tens, if not hundreds, of gigabytes of disk space.

Once an image sequence has been generated, one must methodologically inspect the frames for any noise that are present in the image and filter them out using image processing techniques. In this microfluidic study, the only noise exists in the form of a static sinusoid pattern with a horizontal period of 40 px that is consistent throughout all images. This noise is attributed to the CMOS sensor of the camera and is filtered out using spatial domain filtering based on the Fast fourier transform.

To further enhance an image sequence, a contrast image (Fig. 4(b)) is created from the brightness range of each pixel in an image sequence. This is made possible because the camera is able to stay completely still relative to the microfluidic device. A global thresholding algorithm is applied to the contrast image to create a binary mask, which is then improved topologically through the removal of small (e.g., <100 px) connected matrix components. The improved mask (Fig. 4(c)) is then applied to each image by zeroing out the brightness

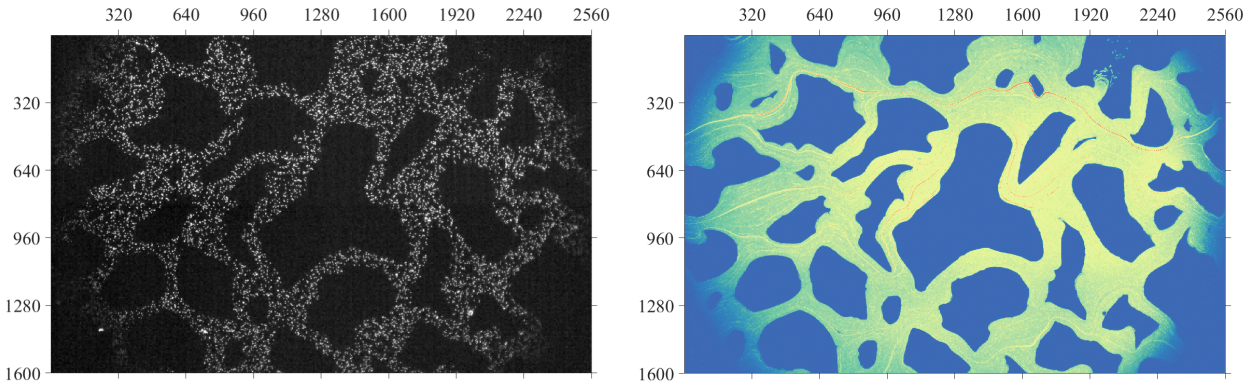

(a) (b)

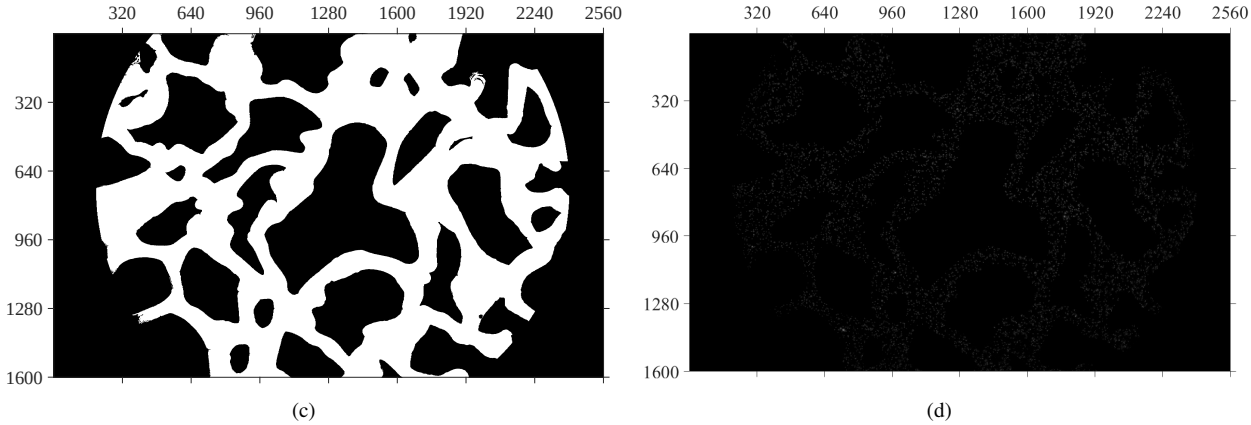

Fig. 4. The preprocessing of frames within each high-speed recording. (a) A frame in an image sequence that has been converted from a cine file. The horizontal sinusoid pattern is visible in the background of this frame, (b) The contrast in brightness level at each pixel throughout a recorded video. For comparison, there are a total of 256 brightness levels in the image format used, (c) A binary mask created from subfigure (b) using simple, automated topological improvements and a circular mask. The dark areas represent two kinds of areas: The matrix, and the edges of the field of vision with low levels of illumination. The bright areas represent the flow channels within the circular mask, (d) A preprocessed frame that has undergone clean-up using spatial domain filtering techniques and the binary mask. The image here is sharper compared to subfigure (a).

of pixels that lie outside the masked (i.e., bright) region and retaining the brightness of pixels that lie within the masked region; (Fig. 4(d)). The image sequence is now ready for processing.

At the beginning of the experiment, injection must be conducted slowly to avoid introducing air bubbles in the permeable medium. Unmoved bubbles are treated as part of the matrix, and do not affect the results. After a few rounds of injection, the fluorescent particles may aggregate in which case the fluorescent solution must be sonicated. A single-exposure, double-frame recording PIV algorithm is used in this study to reconstruct the velocity fields. On a conceptual level, high-density PIV algorithms avoid tracking of individual tracer particles and instead focus on the movement of a collection of particles in close vicinity to each other by deploying a spatial correlation analysis.

3.2 High-density PIV algorithm

The guiding principle of a high-density, single-exposure, double-recording PIV algorithm, as illustrated in Fig. 5, is divide-and-conquer. Each frame is partitioned along each of the two dimensions into non-overlapping interrogation windows that are then cross-correlated with their corresponding search windows in the successive frame. The location of the largest entry in each cross-correlation matrix, called a correlation peak, is indicative of the average displacement of particles in the search window between two adjacent frames. Although a search window may be chosen to have the same size as an interrogation window, it is regarded as best practice to enlarge the search window by at least two times the maximum displacement in each direction along each dimension. In this way, the in-plane loss of pairs is reduced to a level where the correlation peak is highly likely to be meaningful. The output of this PIV algorithm are the components of displacement vectors that are arrangeable in an integer matrix of size $M \times N \times 2 \times (k-1)$. where M and N are the number of interrogation windows along each dimension, 2 is the total number of dimensions, and K is the total number of frames in an image sequence. This matrix is henceforth referred to as the displacement matrix. Take this microfluidic study, for instance, where each 2560×1600 px frame is partitioned into 80×50 interrogation windows, each 32×32 px in size and paired with 64×64 px search windows, ensuring that a maximum displacement of 8 px along each dimension may be reliably calculated.

Even when heeding the aforementioned best practice, a non-negligible percentage of correlation peaks may still be attributed to random noise (i.e., noise peaks) rather than to true displacement (i.e., signal peaks). Displacement vectors due to noise peaks are referred to as spurious vectors because they differ visually from their surrounding neighborhoods when visualized using vector plots. The generation of a smooth vector field may only be accomplished through the removal of spurious displacement vectors. The commonly used normres algorithm based on fluctuation norm identifies the spurious vectors in each frame, which marks the corresponding entries in the output of the PIV algorithm as spurious (Westerweel and Scarano, 2005). As the final post-processing step, components of spurious vectors are replaced by a multi-dimensional interpolation of the valid data along all four dimensions of the displacement matrix. Factoring in the size of the captured area, the resolution, and the frame rate, the displacement matrix may be scaled to become the velocity matrix.

3.3 Quantitative analysis

The velocity field plotted for each frame in an image sequence may be concatenated into a single video. Although it is possible to visually identify accelerations and decelerations in the velocity field by merely watching such videos, it is hard to quantify the exact duration of the transient state unless quantitative indicators of each frame are defined. This microfluidic study uses the mean magnitude of pixel displacement $\overline{|\Delta x|}_k$ averaged over all interrogation windows within the frame k, which is proportional to the average fluid speed for frame

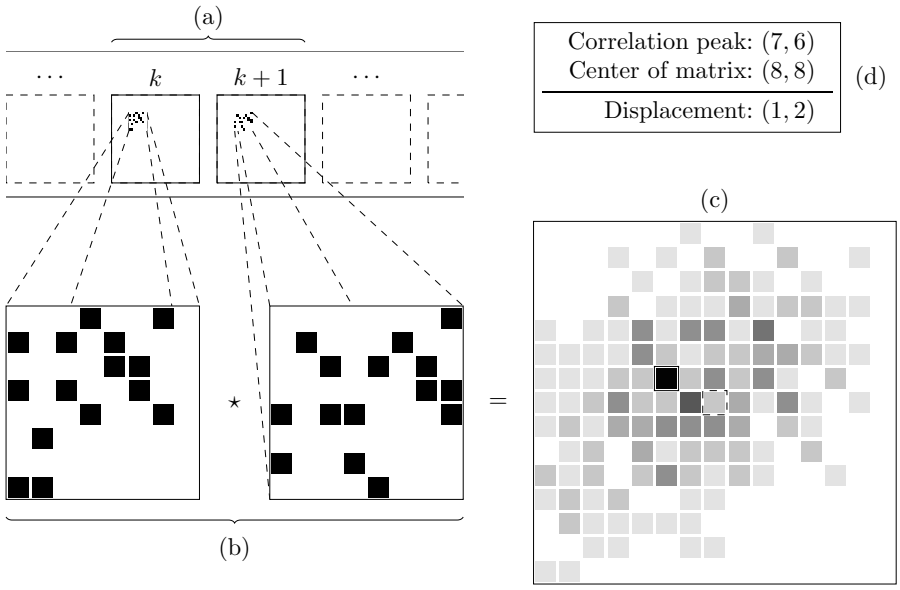

Fig. 5. Illustration of a basic PIV algorithm using (a) forward difference, where the velocity at frame k is calculated from itself and the next frame $k+1$, Frame k is partitioned into non-overlapping interrogation windows, each (b) cross-correlated with a corresponding search window from frame $k+1$ to obtain a (c) cross-correlation matrix. Part (d) shows the index of the correlation peak and the center of the cross-correlation matrix and the most probable displacement in pixel units. For illustration purposes only: The frames have been made binary; the interrogation windows are 8×8 px in size; their corresponding search windows are also 8×8 px in size.

k. A plot of $\overline{|\Delta x|}_k$ against k pixel displacement versus the frame number allows for a quantitative identification of steady states and transient states. The random noise observed in a plot of $\overline{|\Delta x|}$ is indicative of the probabilistic nature of PIV algorithms that lack sub-pixel displacement calculations. By treating notionally identical experiments as a single statistical ensemble, this random noise may be diminished by averaging the $\overline{|\Delta x|}$ response curve obtained from reruns of the same set of experiments. As a final touch, the ensemble plot may be smoothened.

4. Results and discussion

In this section, the experimental results and their interpretation along with possible future improvements to the current work are presented.

4.1 Quantitative results

Two locations are chosen as close as possible to the center of the medium to gather observation data. The first set of experiments, S1-S8, are conducted at the first location, and the second set of experiments, T1-T10, are conducted at the second location. The sudden pressure increase (Δp) used in the first set (i.e., S1-S8) are spaced geometrically to ascertain the effectiveness of the methodology at large flow velocities, and also to establish a reasonable interval of Δp to be in-filled arithmetically by the second set (i.e., T1-T10). For details, see Table 1 and Table 2.

A total of 84 image sequences are recorded with almost half a million frames in total. The quantitative indicator $\overline{|\Delta x|}$ is plotted for each individual experiment and averaged among each set of experiments (see Fig. 6 illustrating S1 and S7. Corresponding figures for S2-6, S8 and T1-10 are included in the Supplementary Information). The indicators for each set of experiments are plotted in the same graph and manually

Table 2. The timestamps of the start and the end of the transient state in each set of experiments.

Set #	Δp (mbar)	k_0	k_1	Δt (s)
S1	10	5	6.67	1.67
S2	20	3.45	4.78	1.33
S3	40	2.5	4.98	2.48
S4	80	2.445	4.95	2.505
S5	160	2.46	4.67	2.21
S6	320	2.46	5.1	2.64
S7	640	2.48	13.54	11.06
S8	1280	3.755	8.957	5.202
T1	100	4	6.7	2.7
T2	200	4	7.05	3.05
T3	300	4	6.78	2.78
T4	400	4	6.855	2.855
T5	500	4	6.35	2.35
T6	600	4	6.635	2.635
T7	700	4	11.15	7.15
T8	800	4	6.545	2.545
T9	900	4	7.875	3.875
T10	1000	3	6.41	3.41

Note: Pressure measurements are precise with 0.1% of the measured values per manufacturer specifications as per (FLUIGENT, 2020).

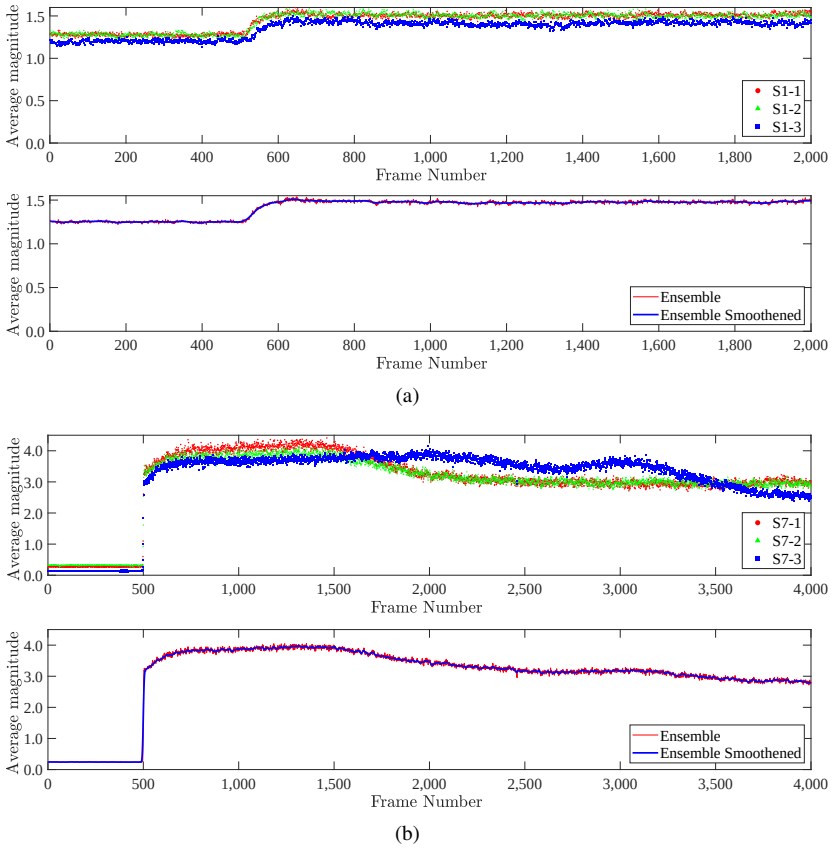

Fig. 6. The average magnitude of displacement in each frame ($\overline{|\Delta x|}_k$, measured in pixels) plotted versus the frame number k for each of the three identical experiments within each set, and as an ensemble average of each set, for the experiments S1 and S7. For S2-6, S8, and T1-10, refer to the Supplementary Information. (a) Experiment S1, Δp = 10 mbar, (b) Experiment S7, Δp = 640 mbar.

aligned so that the start of each transient state is aligned horizontally (see Fig. 7 illustrating S1-S8). The start time, end time, and the duration of each transient state is recorded in Table 2. It is clear from Fig. 6 and Fig. 7 that steady states are identifiable from the $\overline{|\Delta x|}$ plot as horizontal line segments while the transient states are identifiable as curves that connect the horizontal line segments.

Some of the indicator curves display multiple wavefronts, a phenomenon confirmed to exist through simulations of wave propagation in similar domains (Prevost, 1985). Presence of turbulence is ruled out as the responsible mechanism for this phenomenon through manual inspection of high-velocity frames in all image sequences. This phenomenon complicates the reading of the duration of transition states. As a result, the readings for indicator curves that exhibit multiple wavefronts are determined using the frame number by which their second wavefront has been well-diffused. The response time and the stability of the pump are also eliminated as contributing factors to the occurrence of multiple wavefronts per manufacturer specifications (FLUIGENT, 2020).

Duration of transition states are plotted against pressure increases in Fig. 8. Outliers in this dataset are detected by comparing individual residuals with the standard deviation of all residuals for a linear regression model that is fit to all data. Residuals that exceed three times the standard deviation of all residuals for this model are excluded from the dataset and a new linear regression model is fit to the remaining datapoints. For the dataset in Fig. 8, this process is applied twice: The first time, the datapoint highlighted by a rectangle (S7) is removed and the second time, the datapoint highlighted with a triangle (T7) is removed. This results in a robust regression model (Rousseeuw and Leroy, 1987) as shown in Fig. 9. The nonzero slope of the model (P-value = 0.00016) suggests that the duration of transient states is positively correlated with the magnitude of the pressure increase at the inlet (R^2 = 0.65).

4.2 Interpretation

The experimental results confirm the presence of an unsteady state of flow with finite and non-negligible duration when steady single-phase flow conditions in the permeable medium are subject to an instantaneous perturbation in the pressure profile. It is inferred that such scenarios are general features that arise in single- and multi-phase flows in permeable media. Oscillations appear in velocity responses in ensembles of experiments during the transient phase. These oscillations, which are more prominent in experiments with larger perturbations of the pressure gradient, are interpreted using the principle of least action: The fluid phase undergoing perturbation adapts to changes in the pressure profile over a period of time by attempting to establish a velocity field that minimizes the energy dissipation and results in the least flow resistance. It appears that larger changes in the pressure profile

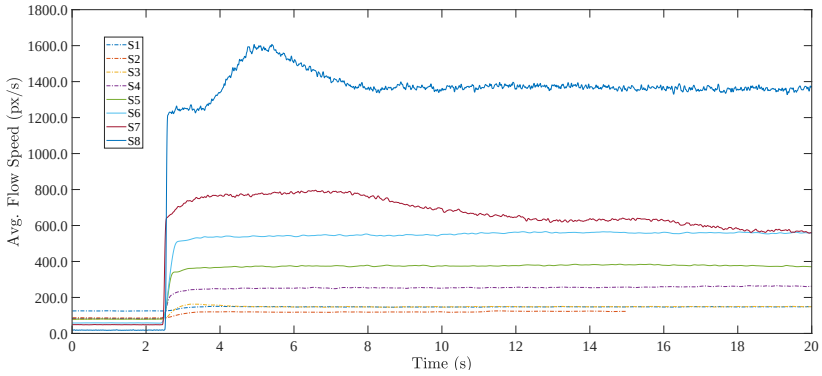

Fig. 7. A smoothened ensemble plot of $\overline{|\Delta x|}_k$ for each set of experiments coded S1-S8. For the experiments coded T, refer to the Supplementary Information.

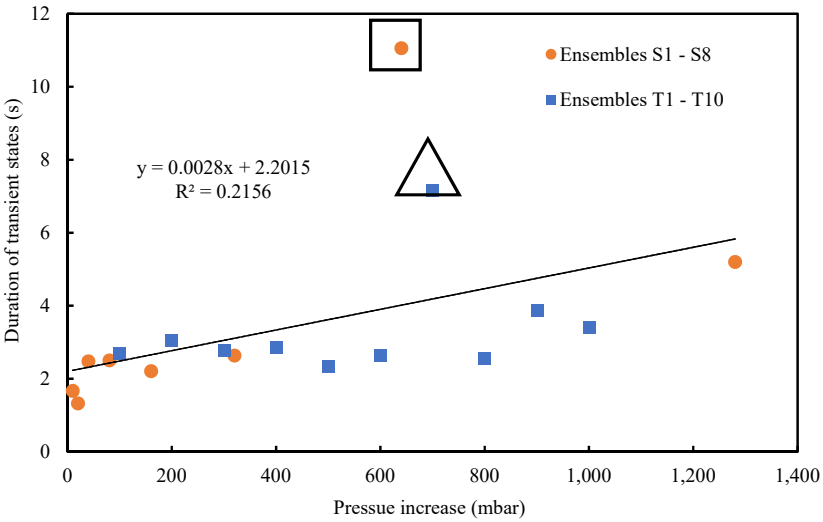

Fig. 8. A scatter plot of the duration of transient states against persistent increases in injection pressure.

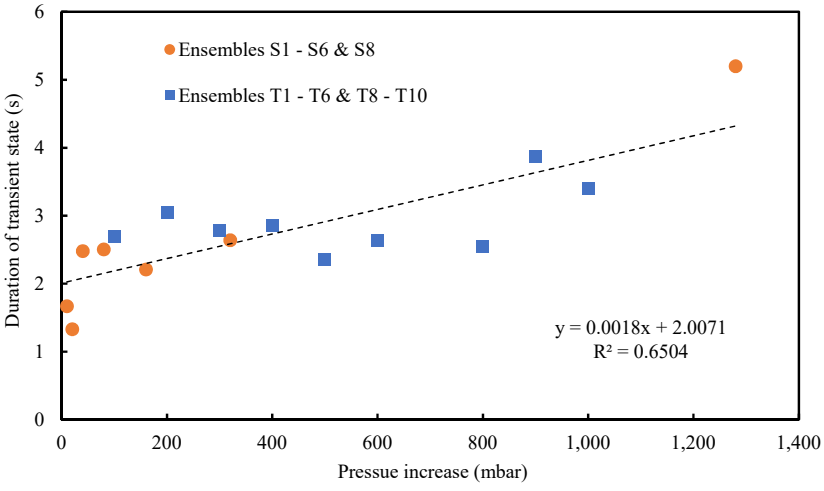

Fig. 9. A scatter plot of the duration of transient states against persistent increases in injection pressure and a fitted linear regression model.

requires more kinematic "effort" to stabilize.

In essence, the fluidic system is minimizing the dissipation of energy by optimizing its flow pathways. This optimization involves a spreading wave that probes the matrix for the optimal distribution of local pressures and the subsequent flow streamlines and velocities. This process takes a finite amount of time, which is quantified in the medium and the fluid used in the experiments. It stands to reason that the size of the medium and the properties of the fluids (e.g., their compressibility and interfacial behavior) may directly affect the duration of this process. That means for much larger systems, these finite transition states may play a significant role in transport behavior and may make flow deviate from the predictions of the classical extension of Darcy's law, especially in unstable flow regimes (Wang et al., 2018). This interpretation has broad implications regarding the applicability of the local steady-state assumption in the numerical simulation of subsurface conditions and provides circumstantial evidence that supports alternative macroscale formulations, e.g., see (Wang et al., 2019).

It is worthwhile to discuss the quality of the input data as well as that of the results, along with potential improvements that may be made upon this microfluidic study. In this work, quality of images is improved significantly using filtering, while the masking of all frames allows the PIV algorithm to ignore search windows that consist entirely of no-flow regions and reduces the occurrence of noise peaks. The basic PIV algorithm implemented in this microfluidic study does not address several issues that may significantly improve the quality of displacement calculations. Future work may leverage improved high-density PIV algorithms in existing literature that feature the following functionalities:

1) Sub-pixel interpolation (Adrian and Westerweel, 2011), which determines sub-pixel movement by analyzing the 3 $\times$ 3 submatrix surrounding each correlation peak, and improves the accuracy of smaller-than-1-px displacements when the dynamic range of the velocity field is high.
2) Multiframe PIV (Hain and Kähler, 2007), which uses central differences (implying errors of second order) and locally adapts to the optimal distance of frames. It is also applicable to a high dynamic range of velocity field and may significantly improve the indicator plot at low flow speeds.

Finally, data postprocessing may be automated. Examples include the alignment of indicator plots and the identification of the start and end time of transient states. Such improvements, which involve the analysis of time series, are left to future work.

5. Conclusions

This article describes in detail a PIV framework for a microfluidic study of single-phase fluid flow in permeable media. The existence of a measurably finite and non-negligible transient state, in the kinematic sense, as a response to the sudden and persistent increase to the pressure drop has been confirmed through the smoothened ensemble average plot of a quantitative indicator. After manual identification of the start and end time of each transition state and excluding outliers, a robust linear regression model was fit to the duration of transient states versus corresponding pressure increases. The nonzero slope of the model suggests that the duration of transient states is positively correlated with the magnitude of the pressure increase at the inlet. The results show the presence of finite and non-negligible transition periods between steady-state flow states by examining single-phase flow of an incompressible fluid in a permeable medium. The present study has important implications for the validity of the fundamental assumption that flowing phases in permeable media relax instantaneously to their steady states. This assumption is the premise for the classical multiphase extension of Darcy's law via constitutive relations that assume local phase equilibrium. The findings in this work point to potential underlying reasons for the lack of predictive capability of the classical macroscale descriptions of multiphase flow in permeable media. The presence of transition flow states may be explained using the principle of least action where reorganization of the velocity field into a new configuration that minimizes the energy dissipation takes a finite amount of time. The results of this paper may be extrapolated to compressible fluids and multiphase flow in permeable media.

Acknowledgement

This work was supported as part of the the center for Mechanistic Control of Water-Hydrocarbon-Rock Interactions in Unconventional and Tight Formations (CMC-UF), an Energy Frontier Research Center funded by the U.S. Department of Energy (DOE), Office of Science, Basic Energy Sciences (BES), under Award DE-SC0019165. The corresponding author thanks Dr. Mohammad Koneshloo for our lively discussions.

Conflict of interest

The authors declare no competing interest.

References

Adrian, R. J. Twenty years of particle image velocimetry. Experiments in Fluids, 2005, 39: 159-169.

Adrian, R. J., Westerweel, J. Particle Image Velocimetry. Cambridge, U.K., Cambridge University Press, 2011.

Aryana, S. A., Kovscek, A. R. Experiments and analysis of drainage displacement processes relevant to carbon dioxide injection. Physical Review E, 2012, 86: 066310.

Aryana, S. A., Kovscek, A. R. Nonequilibrium effects and multiphase flow in porous media. Transport in Porous Media, 2013, 97: 373-394.

Barenblatt, G. I., Patzek, T. W., Silin, D. B. The mathematical model of nonequilibrium effects in water-oil displacement. Paper SPE 75169 Presented at the SPE/DOE Improved Oil Recovery Symposium, Tulsa, Oklahoma, 13-17 April, 2002.

Berkowski, K. L., Plunkett, K. N., Yu, Q., et al. Introduction to photolithography: Preparation of microscale polymer silhouettes. Journal of Chemical Education, 2005, 82(9): 1365-1369.

Cai, J., Jin, T., Kou, J., et al. Lucas-washburn equation-based modeling of capillary-driven flow in porous systems. Langmuir, 2021, 37(5): 1623-1636.

Chung, B. G., Flanagan, L. A., Rhee, S. W., et al. Human neural stem cell growth and differentiation in a gradient-generating microfluidic device. Lab on a Chip, 2005, 5: 401-406.

Dullien, F. A. L. Porous Media: Fluid Transport and Pore Structure. San Diego, USA, Academic Press, 2012.

Elsinga, G. E., Scarano, F. Characterization of PIV systems. Measurement Science and Technology, 2014, 25: 080301.

Ergin, F. G., Watz, B. B., Gade-Nielsen, N. F. A review of planar PIV systems and image processing tools for lab-on-chip microfluidics. Sensors, 2018, 18(9): 3090.

Erickstad, M., Gutierrez, E., Groisman, A. A low-cost low-maintenance ultraviolet lithography light source based on light-emitting diodes. Lab on a Chip, 2015, 15: 57-61.

Guo, F., Aryana, S. A. An experimental investigation of nanoparticle-stabilized CO_2 foam used in enhanced oil recovery. Fuel, 2016, 186: 430-442.

Guo, F., Aryana, S. A. An experimental investigation of flow regimes in imbibition and drainage using a microfluidic platform. Energies, 2019, 12(7): 1390.

Hain, R., Kähler, C. J. Fundamentals of multiframe particle image velocimetry (PIV). Experiments in Fluids, 2007, 42: 575-587.

Hosseini, H., Guo, F., Barati Ghahfarokhi, R., et al. Microfluidic fabrication techniques for high-pressure testing of microscale supercritical CO_2 foam transport in fractured unconventional reservoirs. Journal of Visualized Experiments, 2020, 161: e61369.

Hubbert, M. K. Darcy's law and the field equations of the flow of underground fluids. Transactions of the AIME, 1957, 207(1): 222-239.

King, M. J., King, P. R., McGill, C. A., et al. Effective properties for flow calculations. Transport in Porous Media, 1995, 20: 169-196.

Kubitscheck, U. Fluorescence Microscopy: From Principles to Biological Applications (2nd Edition). New Jersey, USA, Wiley-Blackwell, 2017.

Kvon, A., Lee, Y. H., Cheema, T. A., et al. Development of dual micro-PIV system for simultaneous velocity measurements: Optical arrangement techniques and application to blood flow measurements. Measurement Science and Technology, 2014, 25: 075302.

Li, J., Liu, J., Pei, J., et al. Experimental study of human thermal plumes in a small space via large-scale TR PIV system. International Journal of Heat and Mass Transfer, 2018, 127: 970-980.

Lima, R., Wada, S., Tanaka, S., et al. In vitro blood flow in a rectangular PDMS microchannel: Experimental observations using a confocal micro-PIV system. Biomedical microdevices, 2008, 10: 153-167.

Liu, Y., Kaszuba, J., Oakey, J. Microfluidic investigations of crude oil-brine interface elasticity modifications via brine chemistry to enhance oil recovery. Fuel, 2019, 239: 338-346.

Mijatovic, D., Eijkel, J. C. T., Van den Berg, A. Technologies for nanofluidic systems: Top-down vs. bottom-up—a review. Lab on a Chip, 2005, 5: 492-500.

Murray, C. D. The physiological principle of minimum work: I. The vascular system and the cost of blood volume. Proceedings of the National Academy of Sciences of the United States of America, 1926, 12(3): 207-214.

Northrup, M. A., Kulp, T. J., Angel, S. M. Fluorescent particle image velocimetry: Application to flow measurement in refractive index-matched porous media. Applied Optics, 1991, 30: 3034-3040.

Prevost, J. H. Wave propagation in fluid-saturated porous media: An efficient finite element procedure. International Journal of Soil Dynamics and Earthquake Engineering, 1985, 4: 183-202.

Rousseeuw, P. J., Leroy, A. M. Robust Regression and Outlier Detection. New York, USA, John Wiley & Sons, 1987.

Santiago, J. G., Wereley, S. T., Meinhart, C. D., et al. A particle image velocimetry system for microfluidics. Experiments in Fluids, 1998, 25: 316-319.

Shinohara, K., Sugii, Y., Aota, A., et al. High-speed micro-PIV measurements of transient flow in microfluidic devices. Measurement Science and Technology, 2004, 15: 1965.

Tabeling, P. Introduction to Microfluidics. New York, USA, Oxford University Press, 2005.

Tauro, F., Pagano, C., Porfiri, M., et al. Tracing of shallow water flows through buoyant fluorescent particles. Flow Measurement and Instrumentation, 2012, 26: 93-101.

Thielicke, W., Stamhuis, E. J. PIVlab—towards user-friendly, affordable and accurate digital particle image velocimetry in MATLAB. Journal of Open Research Software, 2014, 2: 30.

Unadkat, H., Rielly, C. D., Hargrave, G. K., et al. Application of fluorescent PIV and digital image analysis to measure turbulence properties of solid-liquid stirred suspensions. Chemical Engineering Research and Design, 2009, 87: 573-586.

Wang, Y., Aryana, S. A., Allen, M. B. An extension of Darcy's law incorporating dynamic length scales. Advances in Water Resources, 2019, 129: 70-79.

Wang, Y., Aryana, S. A., Furtado, F., et al. Analysis of nonequilibrium effects and flow instability in immiscible two-phase flow in porous media. Advances in Water Resources, 2018, 122: 291-303.

Wang, Y., Mckinzie, J., Furtado, F., et al. Scaling analysis of two-phase flow in fractal permeability fields. Water Resources Research, 2020, 56: e2020WR028214.

Westerweel, J., Scarano, F. Universal outlier detection for PIV data. Experiments in Fluids, 2005, 39: 1096-1100.

Whitaker, S. Flow in porous media I: A theoretical derivation of Darcy's law. Transport in Porous Media, 1986, 1: 3-25.

Yi, Y., Blois, G., Kazemifar, F., et al. A particle-based image segmentation method for phase separation and interface detection in PIV images of immiscible multiphase flow. Measurement Science and Technology, 2021, 32: 095208.

FLUIGENT. LineUp Flow EZ. Accessed September 21, 2021.